

# Mapping the magnetic phase diagram of the frustrated metamagnet $\text{CuFeO}_2$

T. T. A. Lummen,<sup>1</sup> C. Strohm,<sup>2,\*</sup> H. Rakoto,<sup>3,†</sup> and P. H. M. van Loosdrecht<sup>1</sup>

<sup>1</sup>Zernike Institute for Advanced Materials, University of Groningen, Nijenborgh 4, 9747 AG Groningen, The Netherlands

<sup>2</sup>Institut Néel, CNRS et Université Joseph Fourier, BP 166, F-38042 Grenoble Cedex 9, France

<sup>3</sup>Laboratoire National des Champs Magnétiques Intenses-Toulouse (LNCMI-Toulouse), 143 Avenue de Rangueil, 31400 Toulouse, France

(Received 21 December 2009; revised manuscript received 19 April 2010; published 14 June 2010)

The magnetic phase diagram of  $\text{CuFeO}_2$  as a function of applied magnetic field and temperature is thoroughly explored and expanded, both for magnetic fields applied parallel and perpendicular to the material's  $c$  axis. Pulsed field magnetization measurements extend the typical magnetic staircase of  $\text{CuFeO}_2$  at various temperatures, demonstrating the persistence of the recently discovered high-field metamagnetic transition up to  $T_{N2} \approx 11$  K in both field configurations. An extension of the previously introduced phenomenological spin model used to describe the high-field magnetization process [T. T. A. Lummen, C. Strohm, H. Rakoto, A. A. Nugroho, and P. H. M. van Loosdrecht, Phys. Rev. B **80**, 012406 (2009)] is applied to each of the consecutive low-field commensurate spin structures, yielding a semiquantitative simulation and intuitive description of the entire experimental magnetization process in both relevant field directions with a single set of parameters.

DOI: 10.1103/PhysRevB.81.224420

PACS number(s): 75.30.Kz, 75.10.Hk, 75.25.-j

## I. INTRODUCTION

One of the richest and most fascinating phenomena in magnetic systems, geometrical frustration, occurs when the specific geometry of an atomic lattice prevents, or frustrates, the simultaneous minimization of all magnetic exchange interactions within the system, thereby inducing a large magnetic degeneracy. With the primary interactions of the magnetic system unable to select a unique magnetic ground state, the magnetic behavior of frustrated systems is dominated by secondary, often weaker interactions, which can vary strongly even across closely related materials. Consequently, the field of frustrated magnetism is characterized by its vast richness and diversity, exotic magnetic states and low-temperature physics.<sup>1-4</sup> One of the classic geometries in which this phenomenon readily manifests itself is the triangular lattice with antiferromagnetic interactions. In absence of significant secondary interactions, classical spins on a triangular lattice antiferromagnet (TLA) compromise in their “desire” to align antiparallel and adopt a noncollinear  $120^\circ$  spin configuration at low temperatures, an underconstrained, highly degenerate ground state.<sup>5,6</sup> The situation can be quite different, however, in systems where secondary interactions are significant, such as in the stacked delafossite material  $\text{CuFeO}_2$ , which consists of hexagonal  $\text{Fe}^{3+}$ ,  $\text{O}^{2-}$ , and  $\text{Cu}^+$  layers (space group  $R\bar{3}m$ ,  $a=b=3.03$  Å,  $c=17.17$  Å). As the  $\text{Fe}^{3+}$  ( $3d^5$ ,  $S=5/2$ ) ions are the system's only magnetic constituents ( $\text{Cu}^+$  and  $\text{O}^{2-}$  have filled electronic shells), and their spins interact antiferromagnetically, the magnetic system corresponds to an archetypical TLA at room temperature [Fig. 1(a)]. Strikingly though, in contrast to other delafossite TLAs such as  $\text{LiCrO}_2$ ,  $\text{AgCrO}_2$ , and  $\text{CuCrO}_2$ ,<sup>5,6</sup>  $\text{CuFeO}_2$  adopts a collinear ground state at low temperatures. Based on the electronic configuration of the  $\text{Fe}^{3+}$  ion ( $^6S_{5/2}$ ,  $L=0$ ), the antiferromagnetic exchange interactions within the system are expected to be isotropic, thus yielding a pure Heisenberg TLA. The presence of a substantial spin-lattice coupling in  $\text{CuFeO}_2$  (the secondary interaction), however, induces a low-temperature structural distortion through the “spin Jahn-

Teller” effect,<sup>7-9</sup> hereby reducing the spin-state degeneracy in the system. The structural symmetry of the  $\text{CuFeO}_2$  lattice is first lowered from the hexagonal  $R\bar{3}m$  space group to the monoclinic  $C2/m$  space group at  $T_{N1} \approx 14$  K, to be further reduced to a lower monoclinic symmetry at  $T_{N2} \approx 11$  K.<sup>10-13</sup> Magnetically,  $\text{CuFeO}_2$  undergoes a transition from its para-

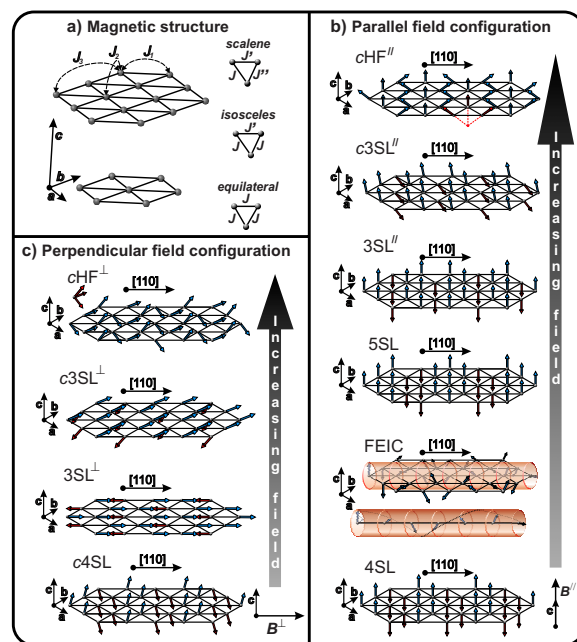


FIG. 1. (Color online) (a) Magnetic structure of  $\text{CuFeO}_2$ , space group  $R\bar{3}m$ ,  $a=b=3.03$  Å,  $c=17.17$  Å. Only the magnetic  $\text{Fe}^{3+}$  ions ( $3d^5$ ,  $S=5/2$ ) are depicted, illustrating the magnetic structure of quasiseparate triangular layers. Different triangular symmetries as consecutively occurring in  $\text{CuFeO}_2$  are depicted on the right. (b) Successively adopted spin structures in the various phases of  $\text{CuFeO}_2$ , when subjected to an increasing applied magnetic field  $B \parallel c$ . The higher field magnetic phases are proposed on the basis of a recently reported classical spin model (PCS model, see text). (c) Analogous sequence of consecutively adopted spin arrangements in  $\text{CuFeO}_2$  for the  $B \perp c$  configuration.

magnetic (PM) phase to a partially disordered, incommensurate (PDIC) magnetic phase at  $T_{N1}$  where a sinusoidally amplitude-modulated magnetic structure with a temperature-dependent propagation wave vector ( $qq0$ ) is adopted.<sup>14,15</sup> Another magnetic phase transition at  $T_{N2}$  brings the system into its collinear four-sublattice (4SL) ground state, in which the spins align (anti)parallel to the  $c$  axis, adopting an in-plane two-up two-down order, as illustrated in Fig. 1(b).<sup>16,17</sup> To avoid confusion, we will refer to crystallographic directions using the hexagonal description depicted in Fig. 1 throughout the paper.

The stabilization of the collinear 4SL state in  $\text{CuFeO}_2$  proved to be one of its most puzzling issues. Initially, the system was described as a two-dimensional Ising TLA with exchange interactions up to the third-nearest neighbors. The first ( $J_1$ ), second ( $J_2$ ), and third ( $J_3$ ) in-plane nearest-neighbor interactions were estimated to compare as  $J_2/J_1 \approx 0.5$  and  $J_3/J_1 \approx 0.75$  in this model<sup>15,17–20</sup> with  $J_1$  corresponding to approximately 1.2 meV.<sup>18,21,22</sup> There is, however, *a priori* no physical justification for the assumed Ising nature of the magnetic moments. Such an assumption is also inconsistent with magnetic-susceptibility measurements, which show highly isotropic behavior above  $T_{N1}$  in  $\text{CuFeO}_2$ .<sup>18,22–24</sup> Nonetheless, the magnetic properties below  $T_{N1}$  are unmistakably strongly anisotropic. The recent discovery of the low-temperature structural distortion offers an alternate picture, as it results in a lattice of scalene triangles in the basal plane [see Fig. 1(a), which splits the first-nearest-neighbor interaction within every triangle into three unequal exchange interactions, lowering the energy of the 4SL state.<sup>10–13</sup> Perhaps more importantly, the distortion has been argued induce a small easy-axis anisotropy along the  $c$  axis as well, further stabilizing the collinear ground state.<sup>25</sup> Experimentally, a small single-ion anisotropy interaction was estimated by fitting a three-dimensional Heisenberg Hamiltonian with a single-ion anisotropy term to the spin-wave dispersion along the  $c$  axis below  $T_{N1}$ , which supports the picture of distortion-induced anisotropy.<sup>21,26</sup> As will be confirmed below, the combination of this weak magnetic anisotropy and the relatively strong spin-phonon coupling in  $\text{CuFeO}_2$  can explain its observed Ising-type behavior.<sup>9,27</sup> Arguably the most fascinating physical properties arise when  $\text{CuFeO}_2$  is subjected to an external magnetic field below  $T_{N2}$ . Upon increasing applied magnetic field along the  $c$  axis ( $B \parallel c$ ), the material has been shown to undergo a series of magnetic transitions at  $B_{c1}^{\parallel} \approx 7$  T,  $B_{c2}^{\parallel} \approx 13$  T,  $B_{c3}^{\parallel} \approx 20$  T,  $B_{c4}^{\parallel} \approx 34$  T, and  $B_{c5}^{\parallel} \approx 53$  T, before ultimately reaching saturation around  $B_{sat}^{\parallel} \approx 70$  T.<sup>18,22,24,25,27–31</sup> Corresponding magnetic structures between the successive transitions [see Fig. 1(b)] were shown to be a proper helical magnetic order with an incommensurate in-plane wave vector, which also carries a ferroelectric moment<sup>24,32–34</sup> ( $B_{c1}^{\parallel} < B^{\parallel} < B_{c2}^{\parallel}$ , ferroelectric incommensurate (FEIC)), and a collinear five-sublattice (5SL) phase where the spins again align (anti)parallel to the  $c$  axis, adopting a three-up two-down order ( $B_{c2}^{\parallel} < B^{\parallel} < B_{c3}^{\parallel}$ ).<sup>28,35</sup> Spin structures at higher fields have not yet been experimentally determined due to the demanding experimental requirements. In a recent work, we have reported pulsed field magnetization measurements, revealing

the retrieval of virtually isotropic magnetic behavior above an additional phase transition at  $B_{c5}^{\parallel}$ .<sup>27</sup> A corresponding anomaly was subsequently observed at somewhat lower fields in pulsed-field ultrasonic velocity measurements by Quirion *et al.*,<sup>31</sup> confirming its proposed magnetoelastic nature. On the basis of a phenomenological classical spin (PCS) model, the spin structures in the high-field magnetic phases were suggested to correspond to a collinear three-sublattice ( $3\text{SL}^{\parallel}$ ,  $B_{c3}^{\parallel} < B^{\parallel} < B_{c4}^{\parallel}$ ), an anisotropic *canted* three-sublattice ( $c3\text{SL}^{\parallel}$ ,  $B_{c4}^{\parallel} < B^{\parallel} < B_{c5}^{\parallel}$ ), and an isotropic *canted* high-field magnetic order ( $c\text{HF}^{\parallel}$ ,  $B^{\parallel} > B_{c5}^{\parallel}$ ), as depicted in Fig. 1(b).<sup>27</sup>

Illustrating the low-temperature anisotropy in the material, the magnetism in  $\text{CuFeO}_2$  evolves quite differently when it is subjected to a magnetic field perpendicular to the  $c$  axis ( $B \perp c$ ) below  $T_{N2}$ , showing only two transitions up to 40 T, at  $B_{c1}^{\perp} \approx 24$  T and  $B_{c2}^{\perp} \approx 30$  T.<sup>18,22,25,28</sup> Our recent results also revealed a high-field magnetic transition for this field configuration, at  $B_{c3}^{\perp} \approx 51.6$  T.<sup>27</sup> Apart from the low-field 4SL structure, the corresponding magnetic structures have not yet been experimentally determined. Based on the magnetization measurements and the aforementioned PCS model, the magnetic structure has been proposed to undergo consecutive spin rearrangements from a *canted* 4SL order ( $c4\text{SL}^{\perp}$  with spins tilted away from the  $c$  direction) to a collinear 3SL phase ( $3\text{SL}^{\perp}$  with spins in the basal plane) at  $B_{c1}^{\perp}$ , to a *canted* 3SL order at  $B_{c2}^{\perp}$  ( $c3\text{SL}^{\perp}$ ), and finally to the isotropic *canted* high-field configuration ( $c\text{HF}^{\perp}$ ) at  $B_{c3}^{\perp}$  [see Fig. 1(c)].

As is clear from above disquisition, the magnetic behavior of  $\text{CuFeO}_2$  as a function of temperature and applied magnetic field has proven very rich and has yielded unanticipated, fascinating insights. Following our recent results, this work aims to thoroughly map out and extend the intricate  $B$ ,  $T$  phase diagrams of  $\text{CuFeO}_2$  up to 58 T and  $T_{N2} \approx 11$  K, for both for the  $B \parallel c$  and the  $B \perp c$  configuration. Furthermore, by applying the recently introduced PCS model to all commensurate sublattice phases occurring in  $\text{CuFeO}_2$ , an adequate description of the entire experimental magnetization process in both field configurations and an intuitive understanding of the magnetic behavior in  $\text{CuFeO}_2$  is provided.

## II. EXPERIMENTAL

### A. Sample preparation

A high quality, single-crystalline rod of  $\text{CuFeO}_2$  was synthesized using the floating-zone technique, following the procedure described by Zhao *et al.*<sup>23</sup> A  $^{57}\text{Fe}$ -enriched starting material ( $^{57}\text{Fe}_2\text{O}_3$ ,  $^{57}\text{Fe} > 95.5\%$ ) was used in the synthesis to facilitate nuclear forward-scattering experiments described elsewhere.<sup>36</sup> X-ray Laue diffraction was employed to orient the  $\text{CuFeO}_2$  single crystal. Next, small cuboid samples ( $5 \times 1 \times 1$  mm<sup>3</sup>) with long sides oriented parallel (35.9 mg) and perpendicular (42.1 mg) to the crystallographic  $c$  axis, respectively, were prepared from the single crystal. Further characterization, including  $^{57}\text{Fe}$  Mössbauer spectroscopy, Raman spectroscopy, and superconducting quantum interference device (SQUID) magnetometry, also yielded experimental data in excellent agreement with literature on

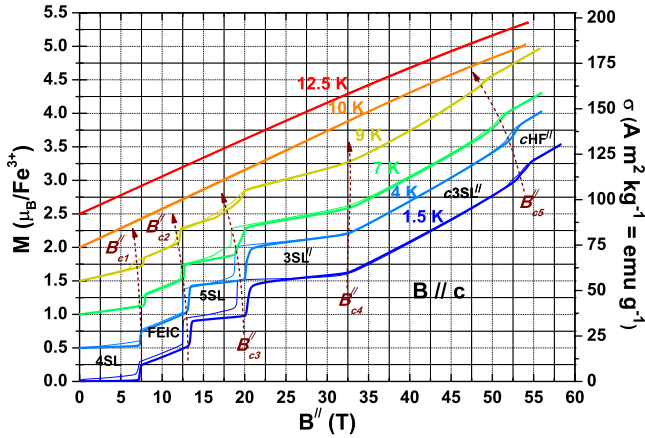


FIG. 2. (Color online) Magnetization measurements in pulsed magnetic fields at various temperatures. The magnetic field is applied in the direction parallel to the  $c$  axis. The various curves are offset by consecutive multiples of  $0.5\mu_B/\text{Fe}^{3+}$  with increasing temperature for clarity. Thick and thin lines represent sample magnetization in increasing and subsequently decreasing magnetic field, respectively. Dashed arrows indicate the temperature dependence of the various magnetic transitions (see also Fig. 3).

$\text{CuFeO}_2$ , confirming the high sample quality. The same samples were used in all measurements reported here and in a previous work.<sup>27</sup>

### B. Instrumentation

High (pulsed) magnetic field magnetization measurements up to a maximum field of 58.3 T were performed at the “Laboratoire National des Champs Magnétiques Pulsés” in Toulouse, France. The obtained magnetization data were accurately scaled through a least-squares fit to low-field measurements (up to 10 T), performed on a well-calibrated static (dc) magnetic field setup (using the extraction technique) of the “Institut Néel” in Grenoble, France. The accuracy in the scaling procedure was such that it introduces an uncertainty of  $\pm 0.3\%$  in all magnetization values determined from the pulsed field experiments. The temperature dependence of dc magnetic susceptibilities of oriented single-crystalline  $\text{CuFeO}_2$  cuboids was measured in various constant magnetic fields (up to 7 T) using a Quantum Design magnetic property measurement system.

## III. RESULTS AND DISCUSSION

### A. Magnetization in pulsed magnetic fields

#### 1. Parallel field configuration ( $B\parallel c$ )

Figure 2 depicts the magnetization curves up to 58.3 T for various temperatures below  $T_{N1}$ , where the applied magnetic field  $B$  is parallel to the  $c$  axis ( $B\parallel c$ ). As  $B\parallel c$  increases, several successive metamagnetic steps are observed, in excellent agreement with previously reported results.<sup>18,22,24,25,27–31</sup> At 1.5 K, the system shows magnetic phase transitions at  $B_{c1}^{\parallel} \approx 7.2$  T (4SL to FEIC phase transition),  $B_{c2}^{\parallel} \approx 13.0$  T (FEIC  $\rightarrow$  5SL),  $B_{c3}^{\parallel} \approx 19.7$  T (5SL  $\rightarrow$  3SL $^{\parallel}$ ),  $B_{c4}^{\parallel} \approx 32.4$  T

(3SL $^{\parallel} \rightarrow$  c3SL $^{\parallel}$ ), and  $B_{c5}^{\parallel} \approx 53.3$  T (c3SL $^{\parallel} \rightarrow$  cHF $^{\parallel}$ ). The three transitions at lowest critical fields  $B_{c1}^{\parallel}$ ,  $B_{c2}^{\parallel}$ , and  $B_{c3}^{\parallel}$  are all accompanied by large magnetization steps and exhibit significant hysteresis ( $B_{c1\uparrow}^{\parallel} = 7.27$  T,  $B_{c1\downarrow}^{\parallel} = 7.15$  T,  $B_{c2\uparrow}^{\parallel} = 13.44$  T,  $B_{c2\downarrow}^{\parallel} = 12.51$  T,  $B_{c3\uparrow}^{\parallel} = 20.32$  T, and  $B_{c3\downarrow}^{\parallel} = 19.08$  T at 1.5 K), indicating their first-order nature. In contrast, at the fourth magnetic transition ( $B_{c4}^{\parallel} \approx 32.4$  T), the  $M(B\parallel c)$  curve shows only a change in slope, suggesting this transition is of second order, which is consistent with synchrotron x-ray diffraction results.<sup>25,30</sup> The high-field transition at  $B_{c5}^{\parallel}$  is again of first-order nature, as illustrated by its hysteresis:  $B_{c5\uparrow}^{\parallel} = 53.78$  T and  $B_{c5\downarrow}^{\parallel} = 52.88$  T at 1.5 K. The existence of this high-field transition was recently confirmed in ultrasonic velocity measurements<sup>31</sup> and can also be seen in previous magnetization data recorded by Ajiro *et al.*,<sup>18</sup> who measured the magnetization of a powder sample of  $\text{CuFeO}_2$  at 8 K in a single turn coil measurement up to 100 T. Though it is obscured in their  $M, B$  curve, presumably due to the polycrystalline nature of the sample, a clear feature can be seen around  $\sim 52$  T in the corresponding  $(dM/dB)$  vs  $B$  graph.

In the 4SL phase, the magnetization is close to zero, as expected for the two-up two-down structure [Fig. 1(b), 4SL]. In the FEIC phase,  $M$  increases linearly with  $B\parallel c$  as observed before,<sup>22,24,25,27,37</sup> signaling a continuous reorientation of the spin system in the spiral phase [Fig. 1(b), FEIC]. In the 5SL phase,  $M$  is almost constant, at a value approximately equal to one fifth of the  $5\mu_B/\text{Fe}^{3+}$  saturation value, in good agreement with the three-up two-down structure [Fig. 1(b), 5SL]. Between  $B_{c3}^{\parallel}$  and  $B_{c4}^{\parallel}$ ,  $M$  is again almost independent of  $B\parallel c$ , having a value close to one third of the saturation value while between  $B_{c4}^{\parallel}$  and  $B_{c5}^{\parallel}$  the magnetization again increases linearly with  $B\parallel c$ , indicating another continuous reorientation of the spin system. Based on these observations and the PCS model, these phases have been proposed to correspond to a collinear three sublattice [Fig. 1(b), 3SL $^{\parallel}$ , two-up one down] and a canted three-sublattice phase [Fig. 1(b), c3SL $^{\parallel}$ ], respectively.<sup>25,27,30</sup> At  $B_{c5}^{\parallel}$ , the system undergoes another first-order transition, where the magnetization exhibits an abrupt jump. Above  $B_{c5}^{\parallel}$ , the magnetization shows a steady linear increase up to the highest field measured, 58.27 T. At this point  $M$  has taken a value of  $3.54\mu_B/\text{Fe}^{3+}$  (at 1.5 K) close to the  $\approx 3.7\mu_B/\text{Fe}^{3+}$  value for the powder sample measured at 8 K by Ajiro *et al.*<sup>18</sup> As the system has regained isotropic behavior above this transition, the spin structure in this cHF $^{\parallel}$  phase has been proposed to be isotropic, such as, e.g., the canted  $120^\circ$  configuration depicted in Fig. 1(b), where the projection of the spins in the basal plane retains the typical  $120^\circ$  configuration while the out-of-plane spin components grow with  $B\parallel c$ . In their recent paper, Quirion *et al.*<sup>31</sup> proposed a similar, though slightly incommensurate  $120^\circ$ -like spin structure based on Landau free-energy considerations.

As the temperature increases, the general features of the  $M, B$  curve survive, though magnetic steps are broadened over an increasingly wide field range, hysteresis widths are reduced and plateau phases acquire increasing slopes. As the temperature approaches  $T_{N2}$ , the characteristic staircase features of the magnetization smooth out and  $M$  increases (quasi)linearly with  $B$ , deviating from this behavior only at high

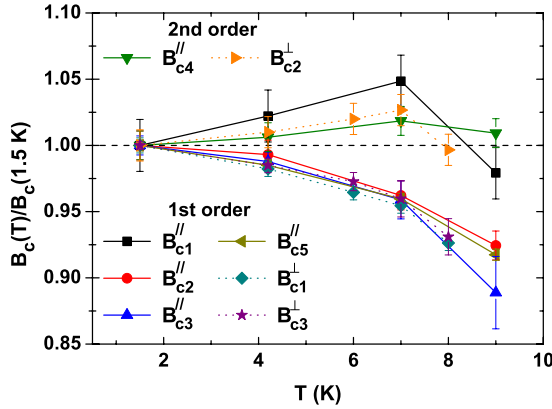


FIG. 3. (Color online) Temperature dependence of the critical fields corresponding to the various magnetic transitions, for both configurations ( $B \parallel c$  and  $B \perp c$ ). Critical-field values (midpoints of hysteresis loop for first-order transitions) are normalized by their corresponding 1.5 K values.

magnetic fields, close to saturation. The fact that this appears to occur already just below  $T_{N2}$  is ascribed to a slight offset of the corresponding temperature sensor at these temperatures, as transition temperatures measured in susceptibility experiments on the same sample (see below) are in accordance with literature values. A striking feature is the temperature dependence of the various magnetic transitions (indicated by the dashed arrows in Fig. 2). Figure 3 shows the relative variation in the corresponding critical magnetic fields with temperature. With the exception of the lowest field-induced transition, all (first-order) transitions exhibiting hysteresis show identical behavior; a continuous decrease in the corresponding critical field ( $B_{c2}^{\parallel}$ ,  $B_{c3}^{\parallel}$ , and  $B_{c5}^{\parallel}$ , respectively) with increasing temperature. In contrast, the critical field of the second-order transition ( $B_{c4}^{\parallel}$ ) proves rather temperature independent, once more indicating its different nature.

## 2. Perpendicular field configuration ( $B \perp c$ )

Figure 4 shows the magnetization process up to 58.3 T for various temperatures below  $T_{N1}$ , for the perpendicular configuration ( $B \perp c$ ). As for the parallel configuration, the magnetization curves are in excellent agreement with earlier observations.<sup>18,22,25,27,28</sup> With increasing  $B^{\perp}$ , the magnetization shows a steady linear increase up to  $B_{c1}^{\perp}$  ( $\approx 24.8$  T at 1.5 K), suggesting a slight continuous canting of the 4SL spins from the  $c$  direction, toward the basal ( $a, b$ ) plane [ $c4SL$ , Fig. 1(c)]. Indeed, neutron-diffraction data have confirmed the stability of this  $c4SL$  magnetic structure up to at least 14.5 T.<sup>28</sup> At  $B_{c1}^{\perp}$ , the system undergoes a first-order magnetic transition to a plateau state, which shows significant hysteresis (at 1.5 K,  $B_{c1\uparrow}^{\perp} = 25.40$  T and  $B_{c1\downarrow}^{\perp} = 24.27$  T). The magnetization in this plateau state is rather independent of  $B^{\perp}$  at an average value of  $\approx 1.53 \mu_B / \text{Fe}^{3+}$ , close to one third of the saturation value, implying a three-sublattice state with spins in the basal plane, directed along  $B^{\perp}$  [Fig. 1(c),  $3SL^{\perp}$ ]. This spin configuration was recently confirmed using numerical minimization of the PCS model.<sup>27</sup> After undergoing a second-order phase transition at  $B_{c2}^{\perp} \approx 30.0$  T (at 1.5 K),  $M$

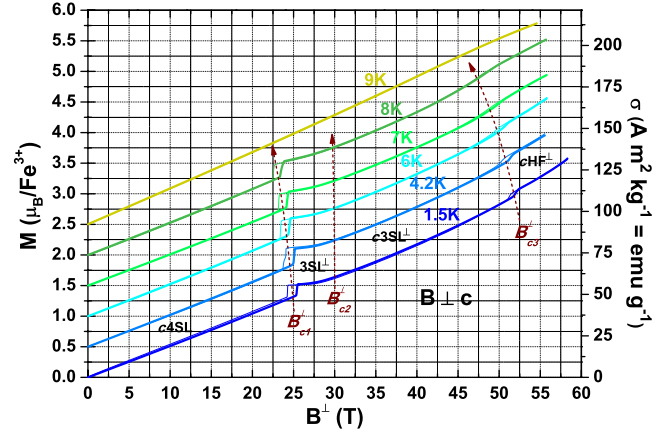


FIG. 4. (Color online) Magnetization measurements in pulsed magnetic fields at various temperatures. Here, the applied magnetic field is perpendicular to the  $c$  direction of the crystal. The various curves are offset by consecutive multiples of  $0.5 \mu_B / \text{Fe}^{3+}$  with increasing temperature for clarity. Thick and thin lines represent sample magnetization in increasing and subsequently decreasing magnetic field, respectively. Dashed arrows indicate the temperature dependence of the various metamagnetic transitions.

once again increases (quasi)linearly with  $B^{\perp}$ , which, in turn, implies a continuous reorientation of the moments away from collinearity. Due to the nonzero easy-axis anisotropy at these fields, the slope in this canted  $3SL$  phase [Fig. 1(c),  $c3SL^{\perp}$ ] differs from that in the same field interval for the parallel configuration. At  $B_{c3}^{\perp} \approx 51.6$  T (1.5 K), another magnetic transition is observed, similar to that at  $B_{c5}^{\parallel}$  in the parallel configuration. As in that configuration, the high-field transition here consists of a first-order metamagnetic step, which exhibits hysteresis (at 1.5 K,  $B_{c3\uparrow}^{\perp} = 52.02$  T and  $B_{c3\downarrow}^{\perp} = 51.18$  T). At 1.5 K,  $M$  jumps to  $\approx 3.1 \mu_B / \text{Fe}^{3+}$  at  $B_{c3\uparrow}^{\perp}$ , after which it resumes a steady increase, in line with a noncollinear spin arrangement. In fact, based on the absence of anisotropy in this canted HF phase ( $cHF^{\perp}$ ), the PCS model predicts a spin structure analogous to that for  $B \parallel c$ , as sketched in Fig. 1(c). The fact that the additional transition occurs at slightly lower critical field in the perpendicular configuration ( $B_{c3}^{\perp} \approx 51.6$  T vs  $B_{c5}^{\parallel} \approx 53.3$  T) explains the broadness of the feature around  $\sim 52$  T in the aforementioned ( $dM/dB$ ),  $B$  curve of the polycrystalline sample of Ajiro *et al.*<sup>18</sup>

With increasing temperature, the general features of the  $M, B$  curve remain intact, although the plateau phase acquires an increasing slope. Furthermore, as for the parallel case, the transition features are smoothed out upon approaching  $T_{N2}$ , and deviation from this behavior only occurs upon approaching saturation. Again, the apparent small temperature mismatch with respect to susceptibility measurements (below) is attributed to a slight offset of the temperature sensor at temperatures close to  $T_{N2}$ . Also for  $B \perp c$ , the temperature dependence of the various critical fields correlates to the nature of the corresponding transitions (see Fig. 3); first-order transitions (at  $B_{c1}^{\perp}$  and  $B_{c3}^{\perp}$ ) exhibit the same relative decrease with temperature as  $B_{c2}^{\parallel}$ ,  $B_{c3}^{\parallel}$ , and  $B_{c5}^{\parallel}$  while the second-order transition (at  $B_{c2}^{\perp}$ ) shows a much weaker temperature dependence.

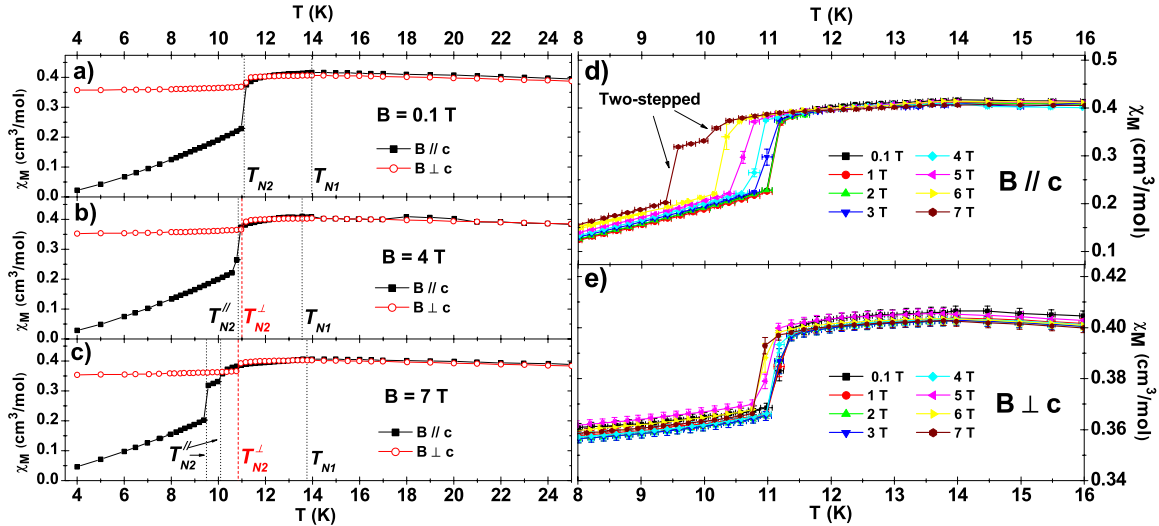


FIG. 5. (Color online) Magnetic susceptibility versus temperature in various constant magnetic fields for both the parallel and the perpendicular configurations. Panels (a)–(c) compare the magnetic susceptibility for  $B \parallel c$  and  $B \perp c$  as a function of temperature at selected fields up to 7 T. Vertical dotted/dashed lines indicate magnetic transition temperatures, as deduced from corresponding  $d\chi_M/dT$  data. The zoom-ins on the data in panels (d) and (e) depict the field dependence of the magnetic susceptibility in parallel and perpendicular configurations, respectively.

3. Progressive symmetry increase

The strong coupling between spin and lattice degrees of freedom is a key ingredient in the description of the magnetization process of  $\text{CuFeO}_2$ . Recently, Terada *et al.*<sup>25,30</sup> showed the strong correlation between the lattice parameters and the magnetization in applied field in both configurations. For  $B \parallel c$ , coinciding with the metamagnetic steps at  $B_{c1}^{\parallel}$ ,  $B_{c2}^{\parallel}$ , and  $B_{c3}^{\parallel}$ , the lattice undergoes corresponding discontinuous contractions along the  $[110]$  direction, while changes in the  $[\bar{1}10]$  direction are much smaller. In addition, the lattice has been shown to increase its symmetry at  $B_{c2}^{\parallel}$ , where the scalene triangle distortion is partially relieved, resulting in a lattice of isosceles triangles [Fig. 1(a)].<sup>12</sup> The lattice parameter along  $[110]$  mirrors the behavior of the magnetization in applied field; within the collinear phases it remains practically constant and in the noncollinear phases the lattice continuously contracts with increasing field (and magnetization). These striking observations can be rationalized as follows: in zero field, the spin-lattice coupling induces the scalene triangle distortion and a magnetic easy axis along the  $c$  direction, thereby reducing the magnetic energy at the expense of elastic energy. As  $B^{\parallel}$  increases, however, a growing tendency for parallel spin alignment in the field direction develops, thereby successively reducing the degree of magnetic frustration (the driving force for the distortion). Thus, as the gain in magnetic exchange energy is successively reduced with  $B^{\parallel}$ , the system rebalances the magnetic and elastic energies associated with the lattice distortion along with every spin rearrangement. As a result, the system exhibits a progressive lattice contraction along  $[110]$ , which mirrors the changes in magnetization.

Since the induced magnetic anisotropy in the material is also directly coupled to the lattice distortion, one may expect the strength of the induced single-ion anisotropy to diminish accordingly with  $M$ , undergoing steps across first order tran-

sitions and continuously decreasing in (*quasi*)linear phases. Indeed, as shown in Fig. 2 of our recent paper,<sup>27</sup> which shows the  $M, B$  curves for both parallel and perpendicular configurations at 1.5 K, the system’s response to an applied field becomes more and more isotropic as  $B$  increases. Moreover, above both high-field transitions, recently confirmed to be magnetoelastic in nature, the system was even found to behave almost completely isotropic, consistent with a vanishing easy-axis anisotropy and the retrieval of an undistorted equilateral triangular lattice.

B. Magnetic susceptibility in constant fields

In order to supplement the magnetic phase diagrams of  $\text{CuFeO}_2$  and to further elucidate its magnetic behavior, the temperature dependence of dc magnetic susceptibilities in various constant magnetic fields was measured in both field configurations. Panels (a)–(c) of Fig. 5 compare the low temperature magnetic susceptibility curves for the two field orientations in applied fields of 0.01, 4, and 7 T, respectively. Consistent with previous measurements, both  $\chi_M^{\parallel}(B \parallel c)$  and  $\chi_M^{\perp}(B \perp c)$  show a diffuse maximum at  $T_{N1} \approx 13.5$  K and a subsequent abrupt drop at  $T_{N2} \approx 11.2$  K upon decreasing temperature.<sup>18,22,23,38</sup> Above  $T_{N2}$  the susceptibility is isotropic, for all applied fields measured. As expected for an ordered antiferromagnet,  $\chi_M^{\parallel}$  approaches zero with decreasing temperature below  $T_{N2}$ , while  $\chi_M^{\perp}$  remains almost constant after the initial drop at  $T_{N2}$ . The field dependence of the magnetic susceptibility, visualized in panels (d) and (e) for parallel and perpendicular configurations, respectively, shows the invariance of  $T_{N1}$  with applied field for both configurations. Though relatively field independent for the perpendicular configuration,  $T_{N2}$  shifts to lower temperatures as the applied magnetic field approaches  $B_{c1}^{\parallel} (\approx 7.2$  T) in the parallel case. This difference can be regarded as a consequence of the lower susceptibility in the ordered phase for

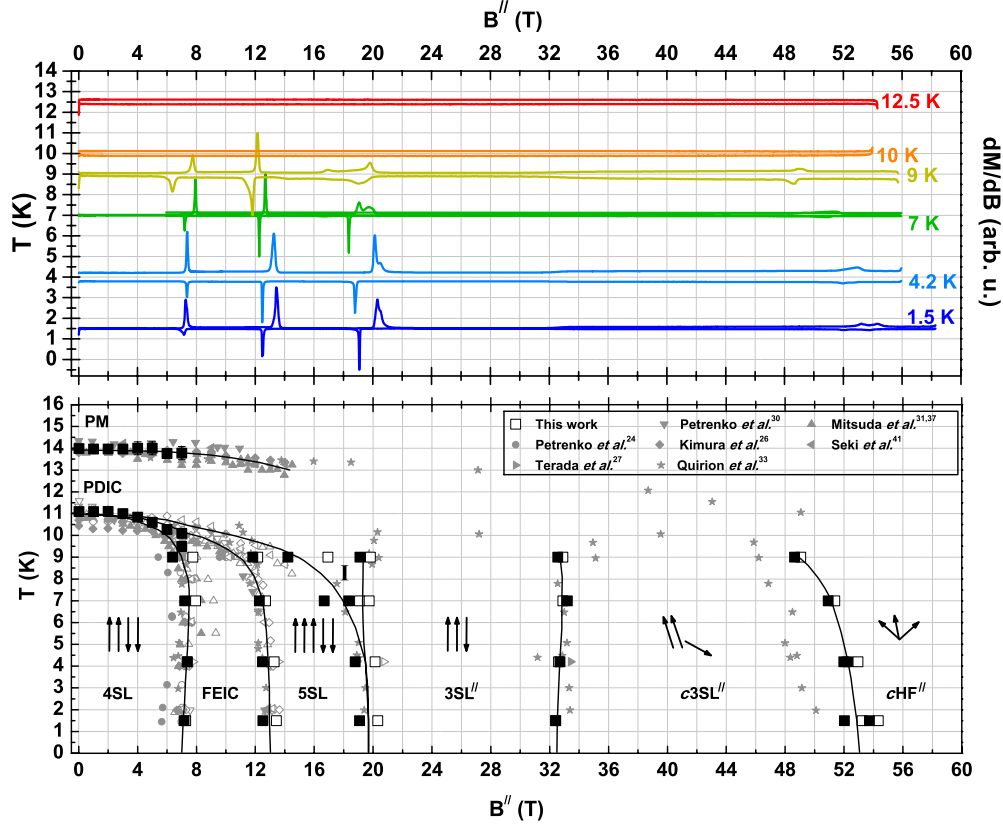


FIG. 6. (Color online) Top panel: differential magnetization curves for  $B\parallel c$ . Colored solid and dotted lines depict (normalized)  $dM/dB$  curves as measured in increasing and subsequently decreasing magnetic field, respectively.  $dM/dB$  curves measured in decreasing magnetic field are inverted for clarity. Additionally, each curve has an offset equal to its corresponding temperature. Lower panel:  $B, T$  phase diagram of  $\text{CuFeO}_2$  for the case where  $B$  is parallel to the  $c$  axis. Large, black squares depict magnetic transitions as observed in this work and smaller gray symbols indicate previously reported transitions. Open and closed symbols represent transitions observed in increasing ( $B$  or  $T$ ) ramps, respectively. Solid lines correspond to proposed phase boundaries. Region  $I$  corresponds to an observed intermediate state (see text).

$B\parallel c$ , which is unfavorable toward the Zeeman interaction, which becomes increasingly strong with  $B$ . Thus, with increasing  $B$  the magnetic ordering transition at  $T_{N2}^{\parallel}$  is shifted to lower temperature. For the perpendicular case, the susceptibility drop across  $T_{N2}^{\perp}$  is only marginal, ergo the corresponding temperature downshift is far less pronounced. As is clear from panels (d) and (e), the transition at  $T_{N2}^{\parallel}$  and 7 T acquires a double feature, indicating the process becomes two stepped. This points toward the presence of an intermediate phase between the two steps. Based on the constructed phase diagram presented below (Fig. 6), this intermediate phase is identified as the helical FEIC phase, as the phase boundaries of both 4SL and FEIC phases bend toward the  $T_{N2}^{\parallel}(B)$  line at these temperatures.

### C. Phase diagrams

With the phase transition data obtained above in hand, the experimental phase diagram of  $\text{CuFeO}_2$  as a function of applied field and temperature can be assembled for both field configurations. Magnetic transition fields and temperatures are defined through the position (center) of corresponding anomalies in the derivatives of the pulsed field magnetization ( $\partial M/\partial B$ ) and susceptibility ( $\partial\chi_M/\partial T$ ) curves, respectively.

Figure 6 shows the  $B, T$  phase diagram for  $\text{CuFeO}_2$  that can be constructed based on aforementioned experiments and other, currently available literature data,<sup>22,24,25,28,29,31,35,39</sup> for the parallel configuration ( $B\parallel c$ ). The diagram features all the previously confirmed phases; the zero-field PM, PDIC, and 4SL phases and the consecutive  $\text{FEIC} \rightarrow 5\text{SL} \rightarrow 3\text{SL}^{\parallel} \rightarrow c3\text{SL}^{\parallel} \rightarrow c\text{HF}^{\parallel}$  phase cascade upon increasing field below  $T_{N2}$ . Worth noting is the fact that the transition from the 5SL to the 3SL phase (at  $B_{c3}^{\parallel}$ ) appears to split up into a two-step transition with temperature, implying an intermediate spin state  $I$ . At temperatures approaching  $T_{N2}$ , the magnetization of the system in the corresponding field region deviates continuously from the 3SL plateau value (see the 7 K line in Fig. 2), suggesting that here (some) spins are canting away from collinearity, before the abrupt rearrangement to the 5SL spin configuration. These double transition features were observed before in steady-state magnetic field measurements up to 23 T,<sup>22</sup> which indicates that this behavior reflects the inherent reduction in the magnetic anisotropy with applied magnetic field in  $\text{CuFeO}_2$ .

Figure 7 shows the analogous  $B, T$  phase diagram resulting from above experiments and earlier reported data<sup>24,25,28,29</sup> for the case where  $B \perp c$ . The diagram includes the zero-field PM, PDIC, and 4SL phases and the field-induced phase cas-

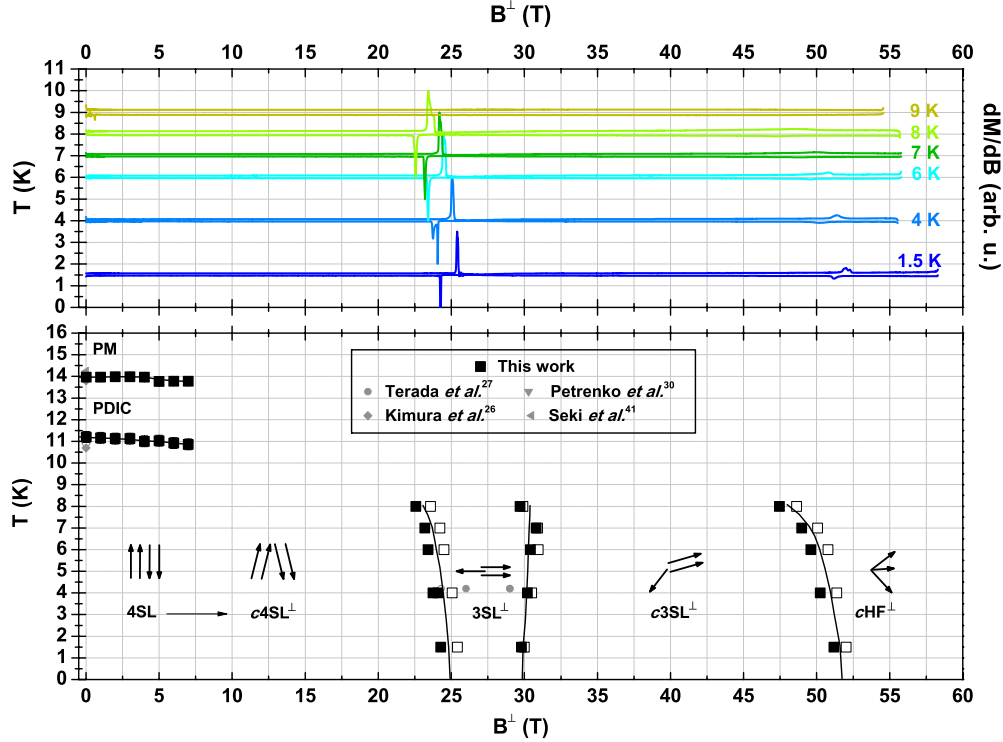


FIG. 7. (Color online) Top panel: differential magnetization curves for  $B \perp c$ . Colored solid and dotted lines depict (normalized)  $dM/dB$  curves as measured in increasing and subsequently decreasing magnetic field, respectively.  $dM/dB$  curves measured in decreasing magnetic field are inverted for clarity. Additionally, each curve has an offset equal to its corresponding temperature for clarity. Bottom panel:  $B, T$  phase diagram of  $\text{CuFeO}_2$  for the  $B \perp c$  case. Large, black squares depict magnetic transitions as observed in this work and smaller gray symbols indicate previously reported transitions. Open and closed symbols represent transitions observed in increasing and decreasing ( $B$  or  $T$ ) ramps, respectively. Solid lines correspond to proposed phase boundaries.

cade for this field configuration:  $c4\text{SL} \rightarrow 3\text{SL}^\perp \rightarrow c3\text{SL}^\perp \rightarrow c\text{HF}^\perp$ .

#### D. Classical spin model

In order to study the magnetization process in  $\text{CuFeO}_2$  further, we resort to the PCS model. This phenomenological model includes the primary magnetic interactions of the system; along with the basic magnetic exchange and Zeeman interaction terms, the strong spin-phonon coupling and the magnetic isotropy in  $\text{CuFeO}_2$  are included. The incorporation of the latter two seems key to capture the Ising-type behavior of the system, as was recently shown.<sup>9,27</sup> To determine the effect of interlayer exchange interactions on the system, these are included in the model separately later.

Spin-lattice interactions are typically incorporated into the Hamiltonian through the distance dependence of the exchange coupling  $J(\mathbf{r})$ .<sup>9,40,41</sup> Ergo, in general, for a system with isotropic exchange interactions the effective Hamiltonian becomes

$$H_{\text{eff}} = J \sum_{\langle ij \rangle} \mathbf{S}_i \cdot \mathbf{S}_j (1 - \alpha u_{ij}) + H_{\text{def}}(\{\mathbf{u}_i\}), \quad (1)$$

where the  $\mathbf{u}_i$  are the displacement vectors, the  $u_{ij} [= (\mathbf{u}_i - \mathbf{u}_j) \cdot \mathbf{r}_{ij} / |\mathbf{r}_{ij}|]$  are the corresponding relative changes in bond length between sites  $i$  and  $j$ ,  $\alpha$  is the spin-lattice constant (to first approximation equal to  $J^{-1} \partial J / \partial r$ ) and  $H_{\text{def}}$  corresponds

to the deformation-energy cost associated with the atom displacements  $\mathbf{u}_i$ , which is thus dependent on the phonon model still to be chosen. Taking the simple bond-phonon model here, which treats the bond lengths  $u_{ij}$  as independent variables, the presence of spin-phonon coupling effectively introduces an additional biquadratic spin interaction of strength  $bJ$ , where  $b = \alpha^2 J / k$  [third term in Eq. (2)].<sup>40,41</sup> Furthermore, since neighboring bond lengths  $u_{ij}$  are independent here, the biquadratic term is restricted to nearest-neighbor couplings only. Due to the quadratic nature of the term, either parallel or antiparallel spin configurations are favorable, which explains the tendency of spin-lattice coupling to stabilize collinear spin states.

Thus, the general spin Hamiltonian (containing only magnetic contributions) for  $\text{CuFeO}_2$  within the PCS model<sup>27</sup> can now be constructed

$$H_s = -g\mu\mathbf{B} \cdot \sum_i \mathbf{S}_i + \sum_{i,j} J_{ij} \mathbf{S}_i \cdot \mathbf{S}_j - \sum_{\langle ij \rangle} bJ_{ij} (\mathbf{S}_i \cdot \mathbf{S}_j)^2 - D(\mathbf{B}) \sum_i S_{iz}^2, \quad (2)$$

where  $\mathbf{B}$  is the applied magnetic field,  $J_{ij}$  is the exchange interaction between sites  $i$  and  $j$ ,  $b$  is the biquadratic coupling constant, and  $D$  is the magnetic-anisotropy constant, which is field dependent due to its strong coupling to the lattice distortion. The Zeeman and anisotropy terms sum

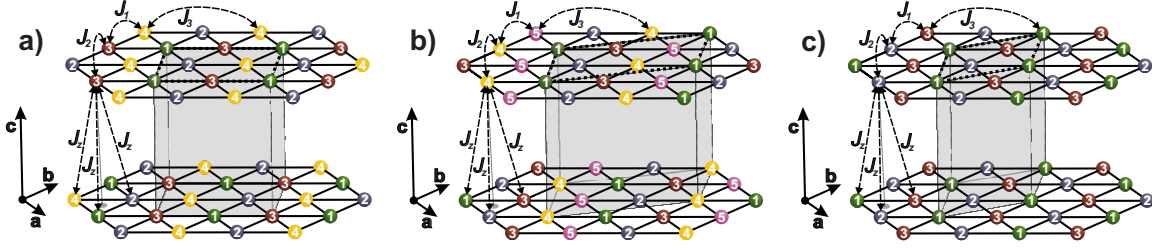


FIG. 8. (Color online) Effective magnetic unit cells in the consecutive (a) four-, (b) five-, and (c) three-sublattice phases of  $\text{CuFeO}_2$ . In all three structures the dotted black lines outline the magnetic unit cell when a single layer is considered (i.e., when  $J_z=0$ ), while the gray shaded volume indicates the effective two-layer magnetic unit cell considered when interlayer interactions are taken into account. Thus, an energetically optimal *ABAB*-type stacking is assumed for each sublattice.

over all sites  $i$ , the biquadratic term couples only nearest-neighbor spin pairs  $i$  and  $j$ , and the exchange term includes all spin-pair interactions in the system.

In a previous work, we analyzed the behavior of this spin Hamiltonian [Eq. (2)] when applied to the magnetic unit cell of the three sublattice structure, thereby focusing on the high-field magnetic phases of  $\text{CuFeO}_2$ . Here, we compare the field dependence of all consecutive commensurate phases, based on the same spin Hamiltonian and the previously extracted parameters. Thus, we evaluate the corresponding spin Hamiltonians for the magnetic unit cells of the four-, five-, and three-sublattice structures on a single triangular sheet; the corresponding unit cells are sketched in Fig. 8. Considering the spins as classical, justified by the large  $S=5/2$  value, we write  $\mathbf{S}_i = e_i S$  (where  $e$  is a unit vector), and  $J_1$ ,  $J_2$ , and  $J_3$  for the first-, second-, and third-nearest-neighbor exchange interactions, respectively. The respective spin Hamiltonians are then found to be

$$\begin{aligned}
 H_{4\text{SL}} = & -2\mu_B \mathbf{S} \mathbf{B} \cdot \sum_i \mathbf{e}_i - D(B) S^2 \sum_i e_{i,z}^2 + 2J_1 S^2 (p_{12} + p_{13} \\
 & + p_{14} + p_{23} + p_{24} + p_{34}) + 2J_2 S^2 (2 + p_{12} + p_{14} + p_{23} \\
 & + p_{34}) + 4J_3 S^2 (1 + p_{13} + p_{24}) - 2AS^4 (p_{12}^2 + p_{13}^2 + p_{14}^2 \\
 & + p_{23}^2 + p_{24}^2 + p_{34}^2), \quad (3)
 \end{aligned}$$

$$\begin{aligned}
 H_{5\text{SL}} = & -2\mu_B \mathbf{S} \mathbf{B} \cdot \sum_i \mathbf{e}_i - D(B) S^2 \sum_i e_{i,z}^2 + 2J_1 S^2 (p_{12} + p_{15} \\
 & + p_{23} + p_{34} + p_{45}) + J_1 S^2 (p_{13} + p_{14} + p_{24} + p_{25} + p_{35}) \\
 & + J_2 S^2 (5 + 2p_{13} + 2p_{14} + 2p_{24} + 2p_{25} + 2p_{35}) \\
 & + 2J_3 S^2 (p_{13} + p_{14} + p_{24} + p_{25} + p_{35}) + J_3 S^2 (p_{12} + p_{15} \\
 & + p_{23} + p_{34} + p_{45}) - 2AS^4 (p_{12}^2 + p_{15}^2 + p_{23}^2 + p_{34}^2 + p_{45}^2) \\
 & - AS^4 (p_{13}^2 + p_{14}^2 + p_{24}^2 + p_{25}^2 + p_{35}^2), \quad (4)
 \end{aligned}$$

$$\begin{aligned}
 H_{3\text{SL}} = & -2\mu_B \mathbf{S} \mathbf{B} \cdot \sum_i \mathbf{e}_i - D(B) S^2 \sum_i e_{i,z}^2 + 3(J_1 + J_3) S^2 (p_{12} \\
 & + p_{13} + p_{23}) + 9J_2 S^2 - 3AS^4 (p_{12}^2 + p_{13}^2 + p_{23}^2), \quad (5)
 \end{aligned}$$

where  $g$  is taken as 2 and spin-spin couplings are written as  $p_{ij} (= \mathbf{e}_i \cdot \mathbf{e}_j)$ . The exchange constants are taken as equal along the different in-plane crystallographic directions, their field dependence being in the spin-phonon term. The spin-phonon

parameter is defined as  $A = bJ_1$ , which corresponds to  $G/3$  in our previous work,<sup>27</sup> though with a rescaled dimensionless biquadratic coupling  $b$  of  $\approx 0.0098$  (here, third-nearest-neighbor interactions are taken into account in the estimation of  $b$ ).

To test the PCS model, we performed numerical minimization of Eqs. (3)–(5) as a function of the independent spin vectors ( $\mathbf{e}_1, \mathbf{e}_2, \mathbf{e}_3, \mathbf{e}_4$ , and  $\mathbf{e}_5$ ) at a given field  $B$ , using previously extracted parameters. In order to incorporate its field dependence, which is *a priori* unknown,  $D$  is approximated to be proportional to  $[M_{\text{sat}} - M(B)]$  here. In other words,  $D$  is assumed to mirror the field dependence of  $M$ , undergoing stepwise reductions at first-order transitions and vanishing as the system approaches saturation; see Figs. 10 and 11. The previously estimated  $D$  for the collinear 3SL phases ( $3\text{SL}^{\parallel}$  and  $3\text{SL}^{\perp}$ ) was  $\approx 0.021$  meV, making it  $\approx 0.031$  meV and  $\approx 0.025$  meV in the collinear 4SL and 5SL phases, respectively. Taking exchange couplings as  $J_1 \approx 0.259$  meV,  $J_2 \approx 0.102$  meV, and  $J_3 \approx 0.181$  meV, and the spin-phonon parameter  $A$  as  $\approx 0.00247$  meV, the parallel-field dependence ( $B \parallel c$ ) of the resulting energy per spin for each of the commensurate sublattice phases is as shown in Fig. 9(a).

Upon examination of the different energy curves, one finds that the PCS model with these parameters yields a cascade of expected magnetic transitions that is consistent with experiment. The 4SL collinear four-sublattice state is stable with respect to the 5SL structure up to  $\approx 9.4$  T. From there on, the 5SL state is the most energetically favorable, up to the critical field  $B_{c3}^{\parallel}$ . Above  $B_{c3}^{\parallel}$ , the collinear  $3\text{SL}^{\parallel}$  state becomes stable, undergoing a transition to the  $c3\text{SL}^{\parallel}$  structure only around  $B_{c4}^{\parallel} \approx 32.4$  T. Experimentally, the multiferroic spiral FEIC phase was found as an intermediate phase, between  $B_{c1}^{\parallel} \approx 7.2$  T and  $B_{c2}^{\parallel} \approx 13.0$  T. As this phase is incommensurate, however, it is not feasible to describe it using the PCS model applied to a limited-size unit cell here. Recently though, such complex incommensurate ground-state structures were found in zero field for far larger unit cells using Monte Carlo simulations.<sup>42,43</sup> Based on the experimental data, the energy per spin of the field-induced FEIC phase in  $\text{CuFeO}_2$  is expected to have a field dependence as indicated by the dotted (green) line in Fig. 9(a), making it the adopted spin structure between  $B_{c2}^{\parallel}$  and  $B_{c3}^{\parallel}$ .

The corresponding magnetization curve for  $B \parallel c$ , depicted in Fig. 10(a), shows a good agreement with the experimental result (Fig. 2, 1.5 K curve). The nondirectional spin-phonon interaction ( $A$ ), which favors collinear spin states, combines

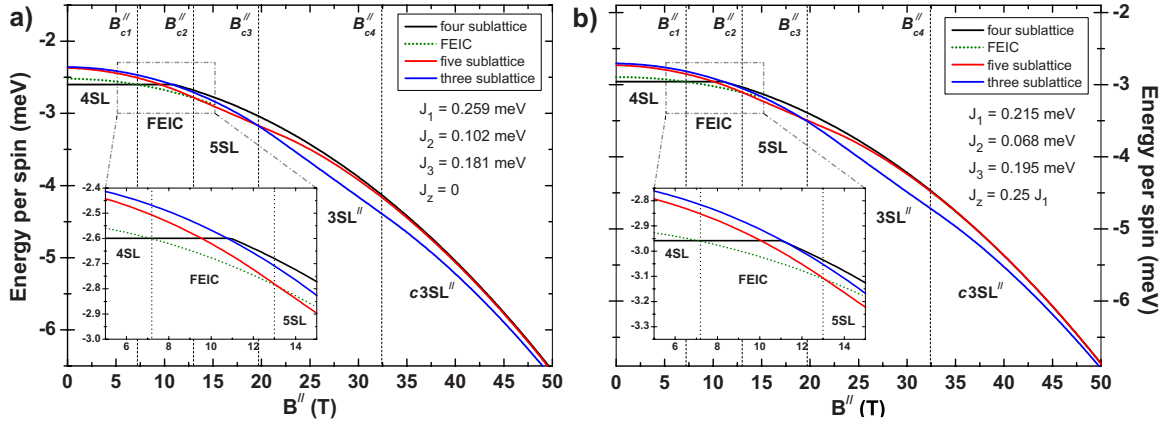


FIG. 9. (Color online) Calculated minimum energy per spin for each of the commensurate sublattice phases ( $B_{\parallel}c$ ) as given by numerical minimization of Eqs. (3)–(5) (a) without and (b) with interlayer exchange interactions. Solid (colored) lines correspond to the four-, five-, and three-sublattice structures, respectively. The dotted green line represents the expected energy per spin of the incommensurate spiral (FEIC) phase. Dashed vertical lines indicate experimental transition fields. Insets show a zoom-in on the 5–15 T region, which features two magnetic phase transitions.

with the directional applied field  $B_{\parallel}$  and the easy-axis anisotropy  $D(B)$  to successively stabilize the consecutive magnetization plateaus of the collinear phases. At high fields (above  $B_{c4}^{\parallel}$ ), the increasingly dominant Zeeman term and the progressively reduced anisotropy result in a gradual spin canting in the system.

In analogous fashion, one can calculate the energy per spin for the commensurate sublattice phases in case of a field applied perpendicular to the  $c$  axis using Eqs. (3) and (5), respectively. Using the same parameters as used for the  $B_{\parallel}c$  case, one obtains an energy scheme as depicted in Fig. 11(a). The  $c4SL$  state is the most energetically favored up to  $B_{c1}^{\perp} \approx 24.8$  T, above which a three sublattice is the most stable, with the spins adopting consecutive  $3SL^{\perp}$  and  $3SL^{\perp}$  structures as the applied field increases. The inset of Fig. 11(a) shows the corresponding simulated magnetization curve for  $B_{\perp}c$  as well as the corresponding assumed value of the magnetic easy-axis anisotropy in the various magnetic phases. The obtained magnetization process is again in good agreement with the experimental curve (Fig. 4, 1.5 K line). As opposed to the  $B_{\parallel}c$  case, the directional anisotropy is

orthogonal to the field direction here, resulting in a much smaller plateau width. Thus, the PCS spin Hamiltonian [Eq. (2)] also provides an adequate description of the low-field part of the magnetization process in  $\text{CuFeO}_2$ , for both field configurations, using the same parameters that were previously used for describing the high-field part.

We emphasize the fact that the spin Hamiltonian parameters used were determined through direct comparison with experimentally observed features. The easy-axis anisotropy  $D$ , only a scaling parameter as  $D(B) \propto [M_{\text{sat}} - M(B)]$ , and spin-phonon coupling  $A$  were determined through the simulation of the high-field magnetization process, which also set the value for the sum of  $J_1$  and  $J_3$ .<sup>27</sup> With these preset restrictions,  $J_2$  and  $J_3$  were set such that: (i) the simulated  $5SL$  to  $3SL^{\parallel}$  transition field for  $B_{\parallel}c$  corresponds to the experimental value ( $B_{c3}^{\parallel}$ ) and (ii) the simulated  $c4SL$  to  $3SL^{\perp}$  transition field corresponds to the experimental  $B_{c1}^{\perp}$  value. The resulting exchange parameters compare as  $J_2/J_1 \approx 0.39$  and  $J_3/J_1 \approx 0.70$ , ratios which are close to those previously estimated.<sup>21,26</sup>

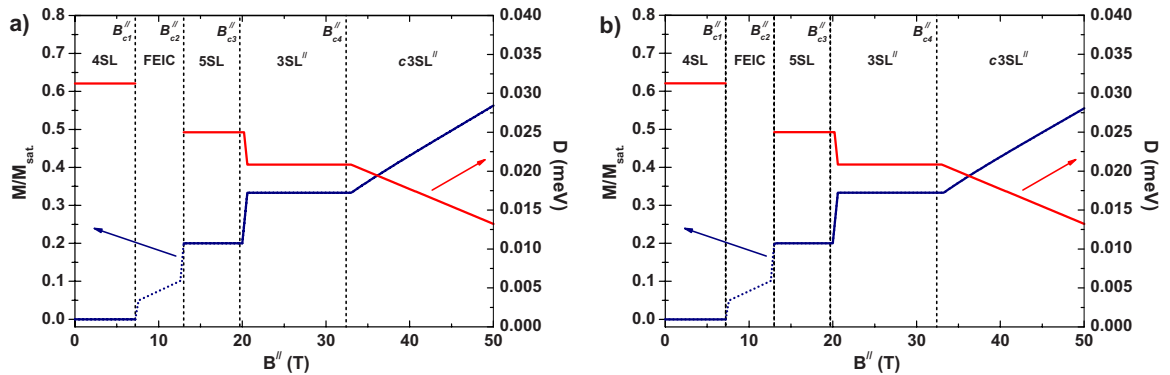


FIG. 10. (Color online) Field dependence ( $B_{\parallel}c$ ) of the magnetization and easy-axis anisotropy in  $\text{CuFeO}_2$  for (a)  $J_z=0$  and (b)  $J_z=0.25J_1$ . Solid blue line: simulated magnetization process of  $\text{CuFeO}_2$  at low magnetic fields (see text). The blue dotted line in the FEIC phase corresponds to the experimental data at 1.5 K (increasing field). Solid red line: corresponding assumed values of the magnetic easy-axis anisotropy in the simulation of the various magnetic phases;  $D$  is approximated to be proportional to  $[M_{\text{sat}} - M(B)]$ .

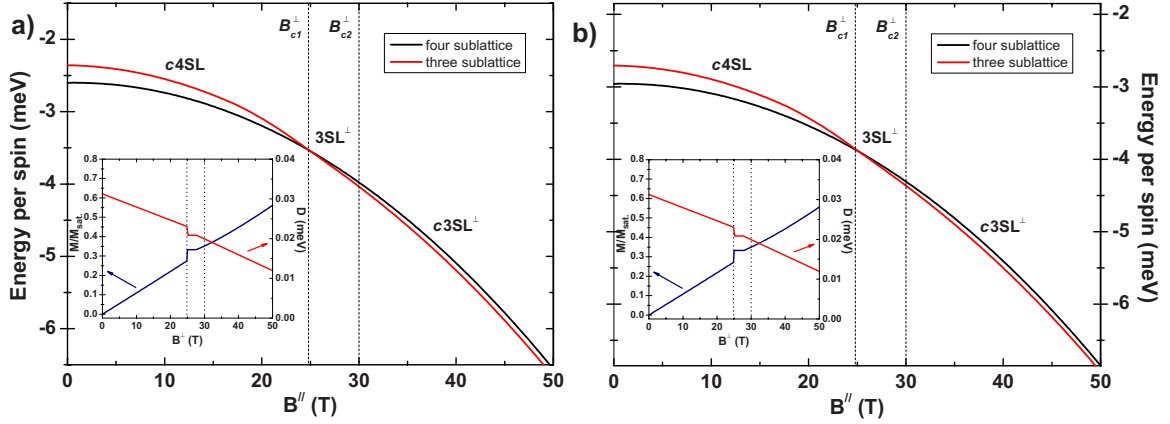


FIG. 11. (Color online) Calculated minimum energy per spin for the commensurate sublattice phases ( $B \perp c$ ) for (a)  $J_z=0$  and (b)  $J_z = 0.25J_1$ . Dashed vertical lines indicate experimental transition fields. Inset: corresponding field dependence of the simulated magnetization (blue) and assumed easy-axis anisotropy (red) in  $\text{CuFeO}_2$  for  $B \perp c$ .

### E. Interlayer exchange interaction

Recent efforts suggest a magnetic-exchange interaction between the Fe layers to be an additional important aspect of the  $\text{CuFeO}_2$  system. Inelastic neutron-scattering work shows indicative spin-wave dispersion along the hexagonal axis, signaling the interlayer interaction to be significant.<sup>21,22,26,44</sup> This is corroborated by the observation of finite dispersion of calculated electronic bands.<sup>45</sup> Thus, here we incorporate the interlayer exchange into the PCS model to determine its influence on the modeled magnetization process. As the interplane interaction is estimated to be small compared to the in-plane exchange, we take a perturbative approach, including only nearest-neighbor interactions ( $J_z > 0$ ). With each spin having nearest-neighbor interlayer couplings to three consecutive sublattice sites in the adjacent layers, all types of stacking of three-sublattice layers are energetically equivalent while four- and five-sublattice layers have specific optimum stacking sequences (those depicted in Fig. 8).<sup>26,46</sup> Assuming this optimal stacking of consecutive layers, the effective magnetic unit cells of the four-, five-, and three-sublattice structures now contain two triangular sheets each, with the additional interlayer interactions amounting to

$$H_{z,4\text{SL}} = 2J_z S^2 (p_{12} + p_{13} + p_{14} + p_{23} + p_{24} + p_{34}), \quad (6)$$

$$H_{z,5\text{SL}} = 2J_z S^2 (p_{13} + p_{14} + p_{24} + p_{25} + p_{35}) + J_z S^2 (p_{12} + p_{15} + p_{23} + p_{34} + p_{45}), \quad (7)$$

$$H_{z,3\text{SL}} = J_z S^2 (3 + 2p_{12} + 2p_{13} + 2p_{23}) \quad (8)$$

per layer. For the collinear sublattice structures these terms add up to  $-J_z S^2$ ,  $-J_z S^2$ , and  $+J_z S^2/3$  per spin for the four-, five-, and three-sublattice structures, respectively. With the inclusion of these terms, Eqs. (3)–(5) were once again numerically minimized to determine optimum spin directions in an increasing field; the resulting energies of the different sublattices and the corresponding simulated magnetization curves are depicted in Figs. 9(b) and 10(b) for  $B \parallel c$  and in Fig. 11(b) for  $B \perp c$ . As is clear from these graphs and their comparison to the case where  $J_z=0$ , the experimental mag-

netization process is equally well simulated upon incorporation of interlayer interactions. Keeping  $A$  and  $D(B)$  at the same value, the incorporation of  $J_z$ , which was fixed at  $0.25J_1$  (a representative value based on inelastic neutron-scattering data<sup>21,26</sup>), results in adapted extracted exchange couplings of  $J_1 \approx 0.215$  meV (making  $J_z \approx 0.054$  meV),  $J_2 \approx 0.068$  meV, and  $J_3 \approx 0.195$  meV. As before, these parameters were determined through direct comparison with observed experimental features of the magnetization process. Though the introduction of an additional antiferromagnetic interaction in the model generally tends to decrease the extracted parameters,  $J_3$  is, in fact, increased here to counter the relative destabilization of the three-sublattice structure. Summarizing, incorporation of interlayer interactions into the PCS model yields an equally adequate description of the experimental magnetization process of  $\text{CuFeO}_2$  with slightly modified exchange parameters.

At this point, it is worth pointing out the limitations of the PCS model presented here. As our calculations focus on minimizing the magnetic energy in specific, chosen sublattice structures, other possible commensurate or incommensurate states are effectively neglected. Calculations on larger magnetic unit cells or triangular lattices with periodic boundary conditions may uncover larger sublattice or more complex spin configurations within the model that may be relevant, as was found to be the case for the zero-field phase of doped  $\text{CuFeO}_2$ .<sup>42,43</sup> The recently proposed incommensurate  $120^\circ$ -like spin structure above  $B_{c5}^{\parallel}$  is one example, though its underlying Landau theory does not capture some general features of the experimental high-field magnetization curve at present.<sup>31</sup> A fully accurate and quantitative description of the magnetism of  $\text{CuFeO}_2$  would require the inclusion of all additional features of the system that could play a role. The incorporation of finite temperature, a more realistic phonon model (yielding longer range biquadratic interactions<sup>9,41</sup>) and quantum spin effects may improve the quantitative understanding of the system. Furthermore, more exotic interactions may play a role in stabilizing the incommensurate spiral state.<sup>47</sup> Nevertheless, the simple PCS model presented here is shown to capture almost all general features of the experimental magnetization process in both field configura-

tions, providing a satisfactory and intuitive description of the observed magnetism in  $\text{CuFeO}_2$ .

#### IV. CONCLUSIONS

Summarizing, we have performed magnetization experiments on  $\text{CuFeO}_2$  at various temperatures below  $T_{N2}$  up to high magnetic fields, both for  $B \parallel c$  and  $B \perp c$  field configurations. The characteristic magnetic staircase of  $\text{CuFeO}_2$  was reproduced and found to retain its general features with increasing temperature below  $T_{N2}$ . As the temperature approaches  $T_{N2}$ , however, transition features are progressively smoothed out and plateau phases are found to acquire increasing slopes. Moreover, the transition from the collinear 5SL to the collinear 3SL<sup>||</sup> phase (at  $B_{c3}^{\parallel}$ ) was shown to split up into a two-step transition near  $T_{N2}$ , revealing an additional, possibly noncollinear, intermediate state *I* at these temperatures. Additionally, the various critical fields of the same nature are shown to exhibit a very similar temperature dependence; all first-order transitions exhibit an analogous relative decrease with temperature, and second-order transitions are found to be relatively temperature independent. Correspondingly, we have thoroughly mapped out the experimental  $B$ ,  $T$  phase diagrams of  $\text{CuFeO}_2$  for both parallel

( $B \parallel c$ ) and perpendicular ( $B \perp c$ ) configurations and expanded them in both temperature and magnetic field. Through numerical minimization of the PCS model applied to the consecutive commensurate sublattice phases of  $\text{CuFeO}_2$ , also the low-field part of the experimental magnetization process was adequately simulated, yielding reasonable estimates for the additional parameters  $J_2$  and  $J_3$ . Incorporation of an additional interlayer exchange interaction in the model was shown to result in a nearly identical simulation and a somewhat adapted set of exchange interactions. Thus, the proposed PCS model, combined with the underlying notion of progressive symmetry increase with applied field, is found to provide a satisfactory semiquantitative description of the entire magnetization process of  $\text{CuFeO}_2$ .

#### ACKNOWLEDGMENTS

The authors would like to thank A. A. Nugroho for his help in the single-crystal growth, T. T. M. Palstra and J. Baas for facilitating use of the optical floating zone furnace and SQUID, and F. de Haan and D. Maillard for technical support. Financial support from the Agence Nationale de Recherche under Contract No. NT05-4\_42463 is gratefully acknowledged.

\*Present address: European Synchrotron Radiation Facility (ESRF), P.O. Box 220, 38043 Grenoble, France.

†Deceased.

<sup>1</sup>A. P. Ramirez, *Annu. Rev. Mater. Sci.* **24**, 453 (1994).

<sup>2</sup>P. Schiffer and A. P. Ramirez, *Comments Condens. Matter Phys.* **18**, 21 (1996).

<sup>3</sup>*Magnetic Systems with Competing Interactions*, edited by H. T. Diep (World Scientific, Singapore, 1994).

<sup>4</sup>J. E. Greedan, *J. Mater. Chem.* **11**, 37 (2001).

<sup>5</sup>H. Kadowaki, H. Kikuchi, and Y. Ajiro, *J. Phys.: Condens. Matter* **2**, 4485 (1990).

<sup>6</sup>M. F. Collins and O. A. Petrenko, *Can. J. Phys.* **75**, 605 (1997).

<sup>7</sup>Y. Yamashita and K. Ueda, *Phys. Rev. Lett.* **85**, 4960 (2000).

<sup>8</sup>O. Tchernyshyov, R. Moessner, and S. L. Sondhi, *Phys. Rev. B* **66**, 064403 (2002).

<sup>9</sup>F. Wang and A. Vishwanath, *Phys. Rev. Lett.* **100**, 077201 (2008).

<sup>10</sup>N. Terada, S. Mitsuda, H. Ohsumi, and K. Tajima, *J. Phys. Soc. Jpn.* **75**, 023602 (2006).

<sup>11</sup>F. Ye, Y. Ren, Q. Huang, J. A. Fernandez-Baca, P. Dai, J. W. Lynn, and T. Kimura, *Phys. Rev. B* **73**, 220404(R) (2006).

<sup>12</sup>N. Terada, Y. Tanaka, Y. Tabata, K. Katsumata, A. Kikkawa, and S. Mitsuda, *J. Phys. Soc. Jpn.* **75**, 113702 (2006).

<sup>13</sup>N. Terada, Y. Tanaka, Y. Tabata, K. Katsumata, A. Kikkawa, and S. Mitsuda, *J. Phys. Soc. Jpn.* **76**, 068001 (2007).

<sup>14</sup>M. Mekata, N. Yaguchi, T. Takagi, T. Sugino, S. Mitsuda, H. Yoshizawa, N. Nobuyoshi, and T. Shinjo, *J. Phys. Soc. Jpn.* **62**, 4474 (1993).

<sup>15</sup>S. Mitsuda, N. Kasahara, T. Uno, and M. Mase, *J. Phys. Soc. Jpn.* **67**, 4026 (1998).

<sup>16</sup>S. Mitsuda, H. Yoshizawa, N. Yaguchi, and M. Mekata, *J. Phys.*

*Soc. Jpn.* **60**, 1885 (1991).

<sup>17</sup>M. Mekata, N. Yaguchi, T. Takagi, S. Mitsuda, and H. Yoshizawa, *J. Magn. Magn. Mater.* **104-107**, 823 (1992).

<sup>18</sup>Y. Ajiro, T. Asano, T. Takagi, M. Mekata, H. A. Katori, and T. Goto, *Physica B* **201**, 71 (1994).

<sup>19</sup>T. Takagi and M. Mekata, *J. Phys. Soc. Jpn.* **64**, 4609 (1995).

<sup>20</sup>S. Mitsuda, T. Uno, M. Mase, H. Nojiri, K. Takahashi, M. Motokawa, and M. Arai, *J. Phys. Chem. Solids* **60**, 1249 (1999).

<sup>21</sup>F. Ye, J. A. Fernandez-Baca, R. S. Fishman, Y. Ren, H. J. Kang, Y. Qiu, and T. Kimura, *Phys. Rev. Lett.* **99**, 157201 (2007).

<sup>22</sup>O. A. Petrenko, M. R. Lees, G. Balakrishnan, S. de Brion, and G. Chouteau, *J. Phys.: Condens. Matter* **17**, 2741 (2005).

<sup>23</sup>T.-R. Zhao, M. Hasegawa, and H. Takei, *J. Cryst. Growth* **166**, 408 (1996).

<sup>24</sup>T. Kimura, J. C. Lashley, and A. P. Ramirez, *Phys. Rev. B* **73**, 220401(R) (2006).

<sup>25</sup>N. Terada *et al.*, *Phys. Rev. B* **75**, 224411 (2007).

<sup>26</sup>R. S. Fishman, F. Ye, J. A. Fernandez-Baca, J. T. Haraldsen, and T. Kimura, *Phys. Rev. B* **78**, 140407(R) (2008).

<sup>27</sup>T. T. A. Lummen, C. Strohm, H. Rakoto, A. A. Nugroho, and P. H. M. van Loosdrecht, *Phys. Rev. B* **80**, 012406 (2009).

<sup>28</sup>O. A. Petrenko, G. Balakrishnan, M. R. Lees, D. M. Paul, and A. Hoser, *Phys. Rev. B* **62**, 8983 (2000).

<sup>29</sup>S. Mitsuda, M. Mase, T. Uno, H. Kitazawa, and H. A. Katori, *J. Phys. Soc. Jpn.* **69**, 33 (2000).

<sup>30</sup>N. Terada *et al.*, *Phys. Rev. B* **74**, 180404(R) (2006).

<sup>31</sup>G. Quirion, M. L. Plumer, O. A. Petrenko, G. Balakrishnan, and C. Proust, *Phys. Rev. B* **80**, 064420 (2009).

<sup>32</sup>T. Arima, *J. Phys. Soc. Jpn.* **76**, 073702 (2007).

<sup>33</sup>T. Nakajima, S. Mitsuda, S. Kanetsuki, K. Prokes, A. Podlesnyak, H. Kimura, and Y. Noda, *J. Phys. Soc. Jpn.* **76**,

- 043709 (2007).
- <sup>34</sup>T. Nakajima, S. Mitsuda, S. Kanetsuki, K. Tanaka, K. Fujii, N. Terada, M. Soda, M. Matsuura, and K. Hirota, *Phys. Rev. B* **77**, 052401 (2008).
- <sup>35</sup>S. Mitsuda, M. Mase, K. Prokes, H. Kitazawa, and H. A. Katori, *J. Phys. Soc. Jpn.* **69**, 3513 (2000).
- <sup>36</sup>C. Strohm *et al.* (unpublished).
- <sup>37</sup>N. Terada, S. Mitsuda, K. Prokes, O. Suzuki, H. Kitazawa, and H. A. Katori, *Phys. Rev. B* **70**, 174412 (2004).
- <sup>38</sup>N. Terada, S. Mitsuda, S. Suzuki, T. Kawasaki, M. Fukuda, T. Nagao, and H. A. Katori, *J. Phys. Soc. Jpn.* **73**, 1442 (2004).
- <sup>39</sup>S. Seki, Y. Yamasaki, Y. Shiomi, S. Iguchi, Y. Onose, and Y. Tokura, *Phys. Rev. B* **75**, 100403(R) (2007).
- <sup>40</sup>K. Penc, N. Shannon, and H. Shiba, *Phys. Rev. Lett.* **93**, 197203 (2004).
- <sup>41</sup>D. L. Bergman, R. Shindou, G. A. Fiete, and L. Balents, *Phys. Rev. B* **74**, 134409 (2006).
- <sup>42</sup>R. S. Fishman and S. Okamoto, *Phys. Rev. B* **81**, 020402(R) (2010).
- <sup>43</sup>J. T. Haraldsen, M. Swanson, G. Alvarez, and R. S. Fishman, *Phys. Rev. Lett.* **102**, 237204 (2009).
- <sup>44</sup>N. Terada, S. Mitsuda, T. Fujii, and D. Petitgrand, *J. Phys.: Condens. Matter* **19**, 145241 (2007).
- <sup>45</sup>V. Eyert, R. Frésard, and A. Maignan, *Phys. Rev. B* **78**, 052402 (2008).
- <sup>46</sup>The five-sublattice structure has other types of optimal stacking which are energetically equivalent.
- <sup>47</sup>M. L. Plumer, *Phys. Rev. B* **78**, 094402 (2008).